



Review

Overview of High-Power and Wideband Radar Technology Development at MIT Lincoln Laboratory

Michael MacDonald ^{*}, Mohamed Abouzahra and Justin Stambaugh

MIT Lincoln Laboratory, Lexington, MA 02421, USA; abouza@ll.mit.edu (M.A.); stambaugh@ll.mit.edu (J.S.)

^{*} Correspondence: mmacdon@ll.mit.edu

Abstract: This paper summarizes over 60 years of radar system development at MIT Lincoln Laboratory, from early research on satellite tracking and planetary radar to the present ability to perform the centimeter-resolution imaging of resident space objects and future plans to extend this capability to geosynchronous range.

Keywords: radar; RCS; ISAR; coherent; integration; Doppler; imaging; tracking; debris; space

1. Introduction

The history of Lincoln Laboratory is intimately tied to that of radar system technology. The Massachusetts Institute of Technology (MIT) established the Radiation Laboratory in 1940 [1] to exploit the British invention of the first practical high-power microwave source, the magnetron, to develop pioneering radar systems for the Allied effort in World War 2. This required the invention of a wide array of microwave technologies, and the Radiation Laboratory ultimately grew to nearly 4000 staff and fielded over 100 different land-, sea- and air-based radar systems which were a decisive factor in achieving Allied victory. When the War ended, the facilities of the Radiation Laboratory were absorbed by MIT.

The establishment of Project Lincoln at MIT in 1951 [2], prompted by Soviet demonstration of nuclear weapons and the capability to deliver them at long range, followed a similar initial history and was co-located at the MIT campus but eventually moved to Hanscom Air Force Base upon the decision to make Lincoln Laboratory an ongoing part of MIT.

Lincoln Laboratory initially fielded radar technology in support of USA efforts to provide an early warning capability against the threat of Soviet nuclear attack via aircraft by means of the Distant Early Warning (DEW) line of modest-sized radars. These radars were capable of tracking aircraft to ~300 km. The MITRE corporation was eventually split from the Laboratory to pursue operational development of these systems.

Later, as the Soviet threat migrated to weapon delivery via intercontinental ballistic missile (ICBM), the Laboratory took a lead role in developing the Ballistic Missile Early Warning System (BMEWS), which required large-aperture, high-power radar systems. Approximately 60 dB greater sensitivity was needed to detect and track warheads having a small radar cross-section (RCS) at ranges of 4500 km.

As a Federally Funded Research and Development Center (FFRDC), Lincoln Laboratory prioritizes the prototyping of advanced technology for national security. That priority is manifested in the history of the Laboratory's radars. The focus of this review will be on the progress made in the area of large-aperture, high-power radar systems from the development of the Millstone Hill Radar (MHR) as a UHF prototype for the BMEWS to the present capability at the Lincoln Space Surveillance Center (LSSC) in Westford, Massachusetts, USA, and the Reagan Test Site (RTS) at Kwajalein Atoll in the Republic of the Marshall Islands. This includes radars operating from UHF (435 MHz) to the W band (96 GHz) with narrowband metric tracking and, in the C band and above, wideband



Citation: MacDonald, M.; Abouzahra, M.; Stambaugh, J. Overview of High-Power and Wideband Radar Technology Development at MIT Lincoln Laboratory. *Remote Sens.* **2024**, *16*, 1530. <https://doi.org/10.3390/rs16091530>

Academic Editors: Vassilis Karamanavis and Piotr Samczynski

Received: 6 December 2023

Revised: 1 March 2024

Accepted: 15 March 2024

Published: 26 April 2024



Copyright: © 2024 by the authors. Licensee MDPI, Basel, Switzerland. This article is an open access article distributed under the terms and conditions of the Creative Commons Attribution (CC BY) license (<https://creativecommons.org/licenses/by/4.0/>).

In 1965, MHR was reconfigured as an L-band (1.295 GHz) radar with a new transmitter and a 12-horn tracking feed [3] it retains to this day. The simultaneous L-band and UHF tracking of satellites led to order-of-magnitude refinements in metric calibration at MHR, which have since been implemented in other radars. The MHR antenna is pictured in Figure 2. The RF front end of the radar is housed in a “doghouse” visible atop the tower. The microwave configuration of the antenna has changed little since its conversion to the L band in the mid-1960s, although the UHF feed has been removed.



Figure 2. The Millstone Hill Radar (MHR) antenna.

The UHF transmitter now serves two different antennas (one fixed at the zenith and a steerable one), which are operated [4] by the MIT Haystack Observatory Atmospheric Sciences Group. This radar operates in Thomson (incoherent) scatter mode to measure

properties of charged particles in the ionosphere, a technique pioneered [5] at Lincoln Laboratory and one requiring a very-large-power–aperture product. This UHF radar is denoted Millstone Incoherent Scatter Radar, and although its name (and history) is co-mingled with that of MHR, they operate today as distinct sensors in separate frequency bands.

MHR pioneered many modern radar capabilities [6,7], such as coherent pulse-to-pulse integration, polarimetric analysis of returns, computer control of the antenna and pulse-by-pulse measurement of target range, antenna-to-target angle error and target velocity in real time.

MHR also serves [8] as a transmit site for multistatic radar demonstrations, most recently with three European receive sites.

A transmitter upgrade, described in Section 3, has been completed and is currently being tested. This will replace the existing obsolescent klystron with a higher average power version with redundant power supply and modulator.

2.2. *The Haystack Planetary Radar (Constructed in 1964, Antenna Replaced in 2014)*

The Haystack antenna was constructed less than a mile from Millstone in 1964 to serve the needs of space communication experiments conducted at the Laboratory and to enable radar measurements with higher range resolution. It was designed for highly efficient operation in the X band (7.84 GHz). This required an exceptionally accurate antenna reflector surface [9]. A 36.6 m diameter antenna was constructed within a 45.7 m radome (a BMEWS spare itself) and configured to a surface accuracy of 10 ppm. The resulting antenna gain was 66 dB, and the associated pencil beam required the antenna pointing to be accurate to within 17 microradians. All of this represented a great leap in the state of the art [10].

Haystack was instrumental in supporting many notable and pioneering science experiments, primary among which was support for the Apollo program, which led to the development of techniques to map the lunar surface. This exploited a technique known as delay-Doppler imaging [11], suitable for rotating objects. The fourth test of general relativity was conducted [12] at Haystack by measuring the time of flight of pulses reflected from Venus as it passed behind the sun to quantify the effect of the solar gravitational field.

In 1970, the MIT Haystack Observatory was created to pursue astronomical research separate from the defense-oriented mission of Lincoln Laboratory. The Haystack facility continued to support both mission areas via its ability to exchange RF boxes through a hoist system which allowed both modalities to be coupled to the antenna, as seen in a cut-away view in Figure 3.

2.3. *The ARPA-Lincoln C-Band Observables Radar (ALCOR; 1970)*

Lincoln Laboratory was tasked [13], in the late 1960s, by the Advanced Research Projects Agency (ARPA) to construct a wideband (512 MHz) C-band (5.67 GHz) radar at the Kiernan Re-entry Measurements System [14] at Kwajalein Atoll. The project was motivated by the need to investigate the physics of ICBM re-entry vehicles (RVs) and the plasma wake they create upon descent through the atmosphere. This radar, ALCOR, required the development of signal processing methods [15] exploiting a “stretch processing” technique [16] by correlation mixing the target return with a replica of the transmit pulse to process it in a much smaller intermediate-frequency (IF) bandwidth.

At the time of its design, it was recognized [17] that some form of time–bandwidth exchange was necessary to process the 512 MHz radar bandwidth in a modest IF bandwidth, and this was accomplished by limiting the range extent, or “window”, of data collection. This was in keeping with ALCOR’s mission to obtain high-resolution signatures on small hardbodies. The need to collect larger datasets motivated the development of a series of analog pulse compressors [18], initially using a cumbersome lumped-element bridged-T network but, in the early 1970s, progressing to an elegant solution via surface acoustic wave (SAW) transversal filters. This implementation proved highly effective and remained in use for 30 years before being supplanted by digital pulse compression techniques during

the Kwajalein modernization and remoting (KMAR) campaign, which implemented the radar open system architecture (ROSA) in the RTS radars. Figure 4 shows the ALCOR antenna inside its radome.



Figure 3. The Haystack antenna as it stood from 1964 to 2014 in a cut-away view. The figures pictured near the subreflector provide a human scale. An RF box can be seen being hoisted into place for insertion at the antenna feed.

ALCOR pioneered inverse synthetic-aperture radar (ISAR) techniques, in which the aspect change of objects as they pass overhead furnishes the Doppler (cross-range) information used to image them. ALCOR obtained the first range-Doppler images [19] of Earth-orbiting satellites.

Figure 5, adapted from [20], shows how an inverse-synthetic-aperture radar (ISAR) image is generated from a time sequence of radar cross-section (RCS), range and Doppler information on individual scatterers. Here, a “dumbbell” of two scatterers is used to illustrate the technique, but it can be extended to the constellation of scatterers which lie within the range “window” over which the radar collects data. As the target changes aspect with respect to the radar, the RCS data are shown in false colors on range–time–intensity (RTI) and Doppler–time–intensity (DTI) plots illustrating how Doppler information resolves the target in the cross-range direction. The integration time is typically chosen to make the resolution in this dimension the same as that in the range dimension. This figure also illustrates that the image plane is the plane in which the target aspect varies.

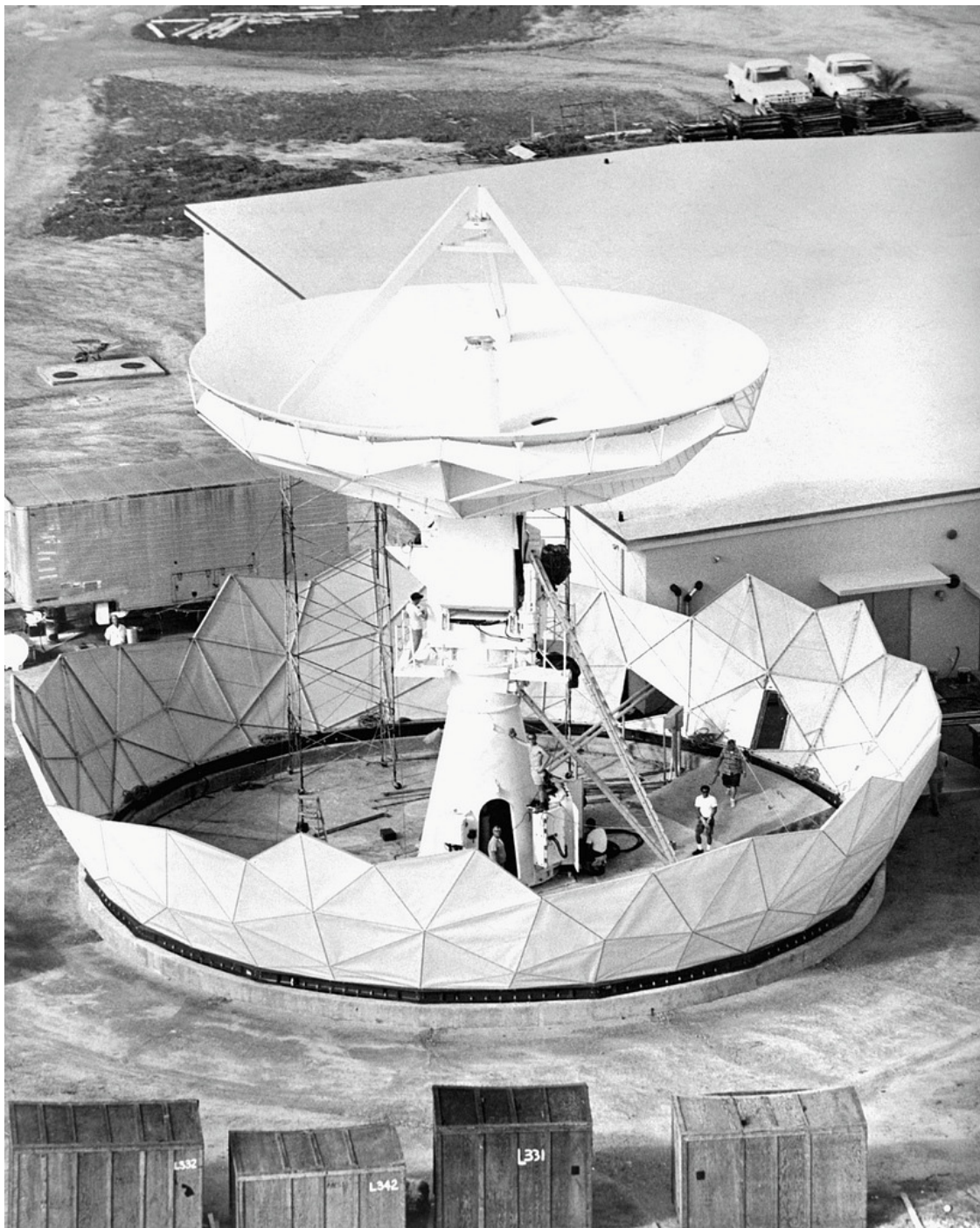


Figure 4. The ARPA-Lincoln C-band Observables Radar (ALCOR) antenna, pictured during its construction in 1968.

A simulated ALCOR image of the Skylab space station resulting from this process is shown in Figure 6. The development of ISAR imaging pioneered at ALCOR has been leveraged by wideband radars described in this paper, such as LRIR, MMW, HAX and HUSIR, as well as other USA assets, and those fielded by other nations, such as TIRA.

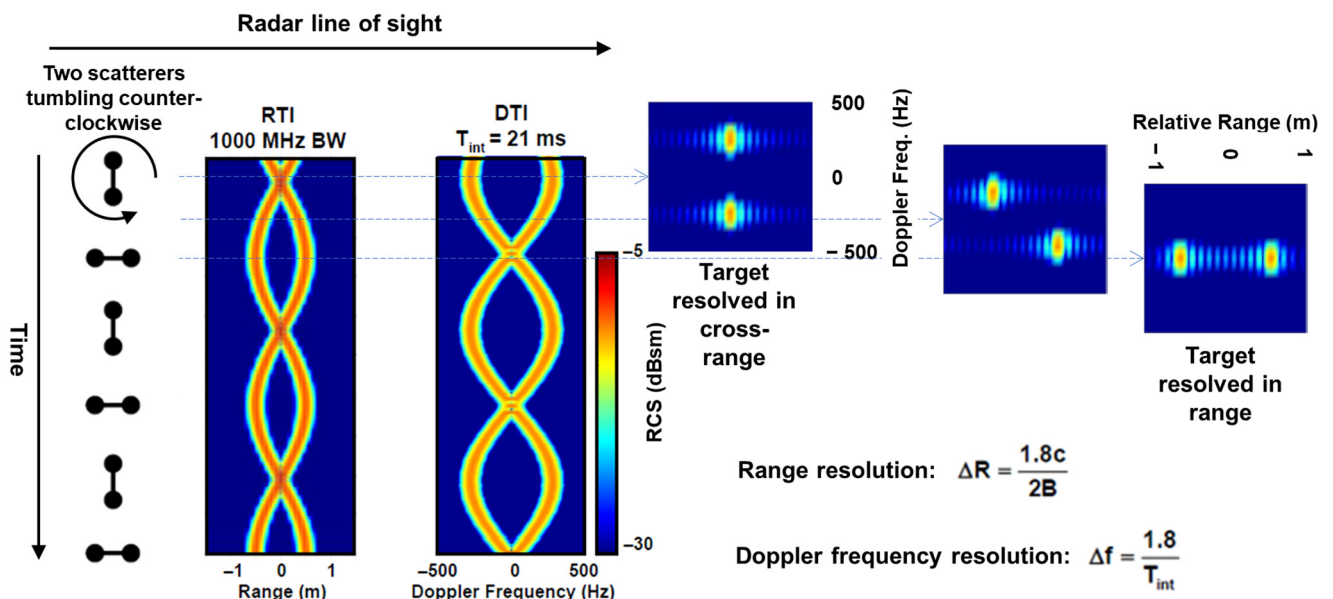


Figure 5. The generation of a range-Doppler image from a time series of range, Doppler and radar cross-section (RCS) measurements of individual scatterers (a dumbbell of two scatterers here).

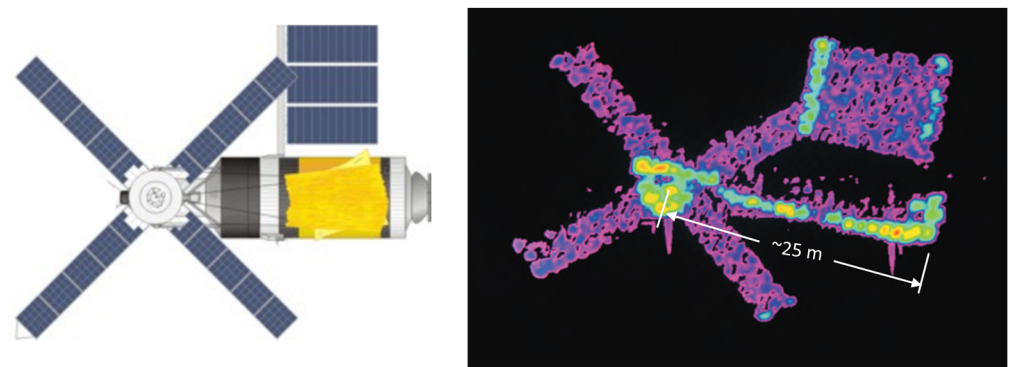


Figure 6. The US Skylab space station, in orbit 1973–1979 (left). A simulated ALCOR image [19] of the Skylab space station illustrating a range-Doppler image (right).

2.4. The Long-Range Imaging Radar (LRIR (1978)/HUSIR-X (2014))

Following the success of ALCOR, the need to extend this satellite imaging capability to geosynchronous range (approximately 40,000 km) became evident, and the Laboratory was again tasked by the ARPA to achieve this. With the large efficient aperture available at Haystack, and the ability to swap the RF box at the antenna which had been a feature of its design, a wideband (1 GHz) high-power and (by necessity) very compact upgrade was implemented in 1978, termed the Haystack Long-Range Imaging Radar [21]. LRIR required technology advances in high-power coupled-cavity traveling wave tube (TWT) technology [22], monopulse tracking feed [23], receiver protection [24] and waveform generation [25]. LRIR also served as a testbed for the deployment [26] of real-time digital processing and control, which was later improved upon and distributed to other radars.

The LRIR feed is illustrated in Figure 7. When the new HUSIR antenna was installed in 2014, its shape, while more accurate, was identical to that of the original Haystack antenna so that no change to the X-band feed was needed. The RF box behind the feed hosts the four X-band coupled-cavity TWT final power amplifiers and their pulse modulator, as well as the four receiver channels (principal-polarized return, orthogonal-polarized return, elevation error and traverse error). The high-voltage power and intermediate-frequency receive chain are routed down the pedestal via cable wraps to a high-voltage power supply and signal processing equipment in the Haystack facility.

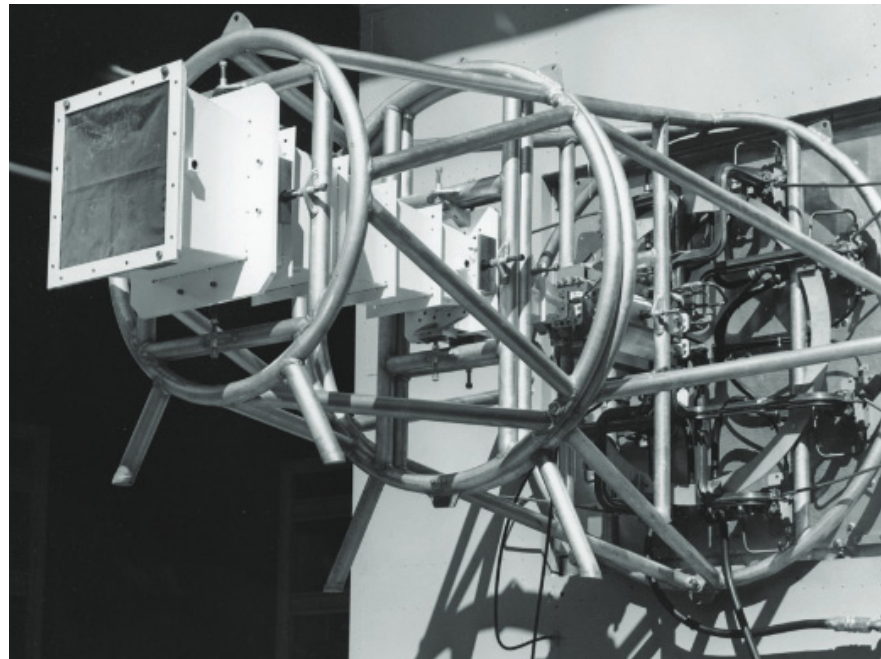


Figure 7. A view of the LRIR feed showing the X-band horn aperture, the support structure and the water-cooled WR28 waveguide.

LRIR has now operated for 45 years and, apart from periodic change-outs of the TWTs (which are lifetime-limited by effects such as occasional high-voltage arcs and, ultimately, depletion of the cathodes), has been a highly reliable sensor. The TWTs developed for LRIR have been employed in other X-band radars since their development.

LRIR has had sufficient sensitivity since its inception to perform the range-Doppler imaging of satellites at geosynchronous range. An upgrade described later plans to bring the W-band capability of HUSIR to this same range. The X-band radar (now referred to as HUSIR-X rather than LRIR, although it is the same sensor) also serves to acquire targets in angle prior to handover to the exceedingly narrow W-band antenna beam.

2.5. The Millimeter-Wave Radar (MMW; Constructed in 1983, Upgraded in 1993 and 2012)

The need to characterize ICBM RVs at millimeter wavelengths at Kwajalein Atoll led to the development of the Millimeter-Wave Radar (MMW) [14]. MMW, whose antenna is shown in Figure 8, was completed in 1983 to gather ballistic missile re-entry signatures in the Ka (35 GHz) and W (95 GHz) bands [27]. The study of re-entry phenomenology at these frequencies was intended to support development of RF seeker technology for ballistic missile defense [28]. Although originally slated to be an adjunct to ALCOR, MMW had sufficient sensitivity to independently track relevant targets with its 25 kW peak-power final-stage Ka-band TWT and monopulse feed, and 1 GHz bandwidth in both the Ka and W bands.

Due to its high operating frequency, the 13.7 m diameter MMW antenna was made with less than 0.1 mm RMS surface tolerance and was also made extremely stiff to support the more than 10 degrees/s angular motion rates needed to track RVs through re-entry at Kwajalein. The antenna was built by Electromagnetic Space Structures Co. (ESSCO; now part of Communications and Power Industries), Ayer, MA USA, which had been spun off from Lincoln Laboratory in the 1960s. The antenna and its 20.7 m diameter radome were placed atop a 12 m high cylinder to elevate it above the treetops and to mitigate the effects of salt spray, which is present in the marine environment of Kwajalein Atoll.



Figure 8. The Millimeter-Wave Radar (MMW) antenna is seen in the foreground as a new GoreTex® radome was installed in 2003.

MMW began providing satellite imagery for the US Space Command in 1988. The ISAR capability at ALCOR and MMW led [29] to the initiation of the Space Object Identification (SOI) mission area at Lincoln Laboratory, which continues to this day. As the highest-resolution radar on Kwajalein Atoll, MMW's role quickly expanded from re-entry signature studies to the ISAR imaging of re-entering and orbiting objects.

The increased demand for high-resolution MMW data motivated numerous major system upgrades throughout the radar's history. At the time of its initial construction, MMW employed a conventional antenna feed structure with an extensive network of water-cooled WR28 and WR10 rectangular waveguides. A drawing of the original microwave system is shown in Figure 9. MMW's Ka-band system underwent a series of major upgrades in 1988–1994, which culminated in the maximum bandwidth being doubled to 2 GHz. These upgrades also increased the radar sensitivity by over 10 dB, tripling the tracking range [27]. These enhancements were due in part to advancements in computing technology and algorithms to improve its real-time coherent tracking and the redesign of the high-power

amplifier by Varian (now Communication and Power Industries), doubling the peak-power output of the TWT to 50 kW, as well as doubling its bandwidth.

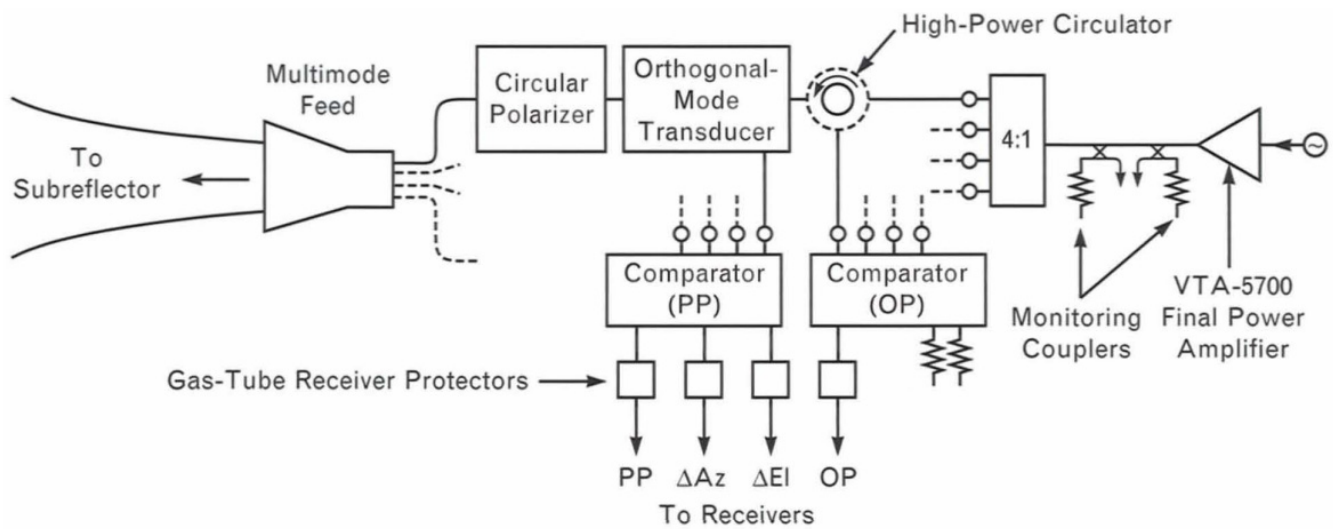


Figure 9. A schematic of the original MMW microwave system (1983).

The high loss of rectangular waveguide at millimeter wavelengths severely limited the achievable sensitivity of the original radar. In 1993, a novel quasi-optical beam waveguide feed was implemented [30], dramatically reducing resistive loss in the transmit feed while enabling the free-space combining of two TWTs with low loss. This effort built upon work that the Laboratory had conducted on submillimeter-wavelength technology employing off-axis paraboloid mirrors turned on a lathe [31]. These mirrors proved suitable for constructing Gaussian beam waveguides [32], in which optical elements such as Faraday rotators [33] could be added to separate the principal-polarized (PP) and orthogonal-polarized (OP) returns. The use of mirrors rather than lenses in the beam waveguide enables high-power operation. An additional advance was the use of a symmetric “clamshell” mirror topology, which effectively cancels the cross-polarization generated [30] by the amplitude asymmetry of a single off-axis paraboloidal mirror. An order-of-magnitude increase in the sensitivity of MMW was achieved while doubling its imaging resolution. The upgraded quasi-optical beam waveguide is shown in Figure 10.

The wideband high-power quasi-optical front end implemented at 35 GHz for MMW was later redesigned for 16.7 GHz for the HAX radar and for 95 GHz for MMW [34] and the Naval Research Laboratory WARLOC radar [35], for which Lincoln Laboratory built the duplexer unit.

The MMW TWT design formulated in 1992 proved difficult to reliably build for Communications and Power Industries (CPI), Palo Alto, CA USA, and the radar sensitivity degraded with time. This, along with the need for improved image resolution, motivated a new coupled-cavity TWT development at CPI, which yielded a new tube having more power than the 1992 design, and an additional two-fold increase in bandwidth. Lincoln Laboratory made an extensive effort [36] to leverage this improvement to upgrade MMW to 4 GHz bandwidth. The linear-FM waveforms employed the existing waveform generator in a dual-chirp configuration to double the bandwidth. The receiver hardware was also extensively modified. The Faraday rotator was redesigned to obtain a seven-fold improvement in its thermal performance, enabling higher-power operation. The HAX polarizer, which functioned over a 12% fractional RF bandwidth, was adapted to 35 GHz to support a similarly wide bandwidth for MMW. This upgrade doubled the image resolution of the radar. Sensitivity enhancements doubled the tracking range of the radar. Improvements in receiver electronics more than tripled the range “window” over which target data are collected. Isolation between the principal- and orthogonal-polarized returns was improved by 16 dB, and the range sidelobe level was improved by 13 dB.

The MMW feed is compatible with the use of quasi-optical quadrature hybrids [32] for TWT power combining [37] by means of a fused quartz disk. Replacing the disk with a metal plate, or omitting it, permits single-TWT operation. The same technique was employed for frequency diplexing, with a perforated metal plate being used for transmission in the W band and reflection in the Ka band for this purpose. Ka-band-only operation could be implemented by means of a flat metal plate. This provides a highly flexible means of adapting the radar to different configurations.

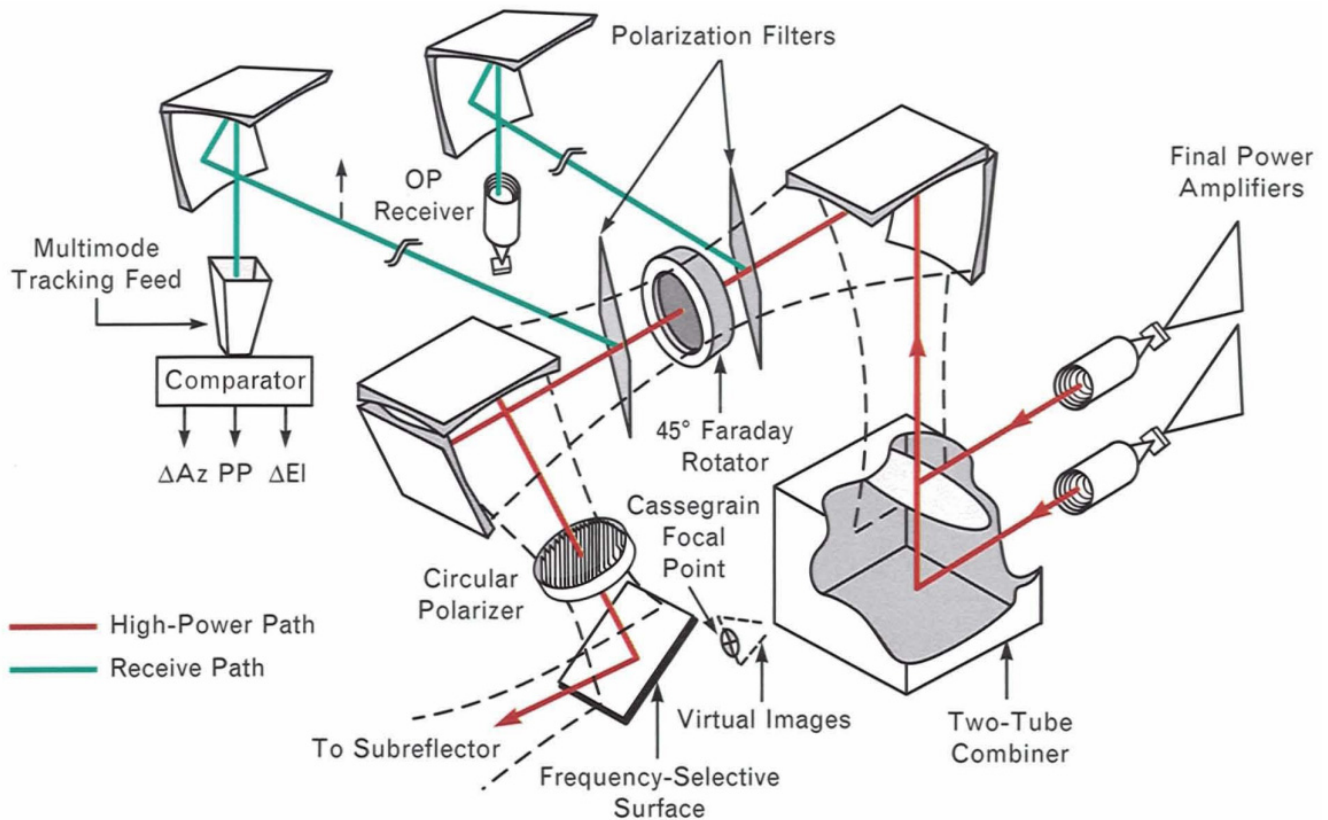


Figure 10. A schematic of the quasi-optical MMW microwave system (1992).

2.6. The Haystack Auxiliary Radar (HAX; 1993)

The Haystack Auxiliary Radar (HAX) was constructed in 1993 to reduce the operational demand on LRIR, which continued to share the Haystack antenna with ongoing radio astronomy activities [38]. HAX complemented LRIR in providing Earth orbiting debris data to NASA [7,39]. The HAX transmitter [40] achieved a 12% fractional bandwidth in the Ku band (16.7 GHz) with the first deployment of the re-entrant double-staggered ladder TWT circuit being invented [41] by Varian (now CPI).

HAX has performed these tasks admirably in terms of satellite imaging and debris characterization. The HAX antenna, pictured in Figure 11, was adapted [42] from an MSC-46 satellite communications antenna originally manufactured by Hughes Aircraft Company. This antenna was extensively modified to improve its pointing and tracking performance and placed in a 20.7 m diameter radome. A quasi-optical beam waveguide similar to that developed earlier for MMW (described in the previous section) was also put in use at HAX to support its 2 GHz bandwidth and high transmit power. A recent redesign of the HAX coupled-cavity TWT by CPI has improved its manufacturability and reliability.



Figure 11. The Haystack Auxiliary Radar (HAX) antenna.

HAX and HUSIR-X continue to jointly be the primary source of the NASA Orbital Debris Program Office [43], with HAX providing shorter-wavelength operation and a wider field of view than HUSIR-X.

The Ku-band vacuum electronics technology developed by CPI for HAX has also found use at the Fraunhofer Institute for High Frequency Physics and Radar Techniques (FHR) Tracking and Imaging Radar (TIRA), which has been extensively used [44,45] for the ISAR imaging of space objects, an example of which is seen in Figure 12.

2.7. The Cobra Gemini Radar (1996) and the XTR-1 Radar (2012)

A need for a transportable dual-band (S and X) radar led to the development of the Cobra Gemini radar [46] at the Laboratory in 1996. The radar open system architecture (ROSA) developed for Cobra Gemini [47] was later distributed to other USA radars at Kwajalein Atoll and to Lincoln Laboratory radars at the LSSC as a common real-time processing architecture, greatly streamlining operations and maintenance needs. It has been further extended [48] to support net-centricity for networked Department of Defense (DOD) needs. Cobra Gemini incorporated motion-compensation techniques, allowing it to be deployed on a T-AGOS class ship. This successful development program led to that of the X-band Transportable Radar (XTR-1) in 2012 [49]. XTR-1 has a significantly larger antenna (11 m diameter) [50] than Cobra Gemini (4.5 m diameter).

2.8. Haystack Ultra-Wideband Satellite Imaging Radar (HUSIR-W; 2014)

Following the previously described and highly successful developments, an ambitious program to implement 8 GHz bandwidth for high-resolution ISAR satellite imaging was achieved in 2014 with the commissioning of the Haystack Ultra-Wideband Satellite Imaging Radar (HUSIR) [51]. The LRIR X-band capability was retained, while the Haystack 37 m reflector was replaced [52], and its shape holographically optimized [53] to accommodate

operation in the 92–100 GHz band with a new transmitter [54] and signal processing [55]. HUSIR also retains the ability for the MIT Haystack Observatory to perform astronomical observations with the new antenna [56] and supports continued orbital debris measurements for NASA [57]. It has also found use as a high-power source for terrestrial RF power beaming demonstrations [58]. In 2014, the project was awarded an “R&D 100” prize from R&D Magazine.

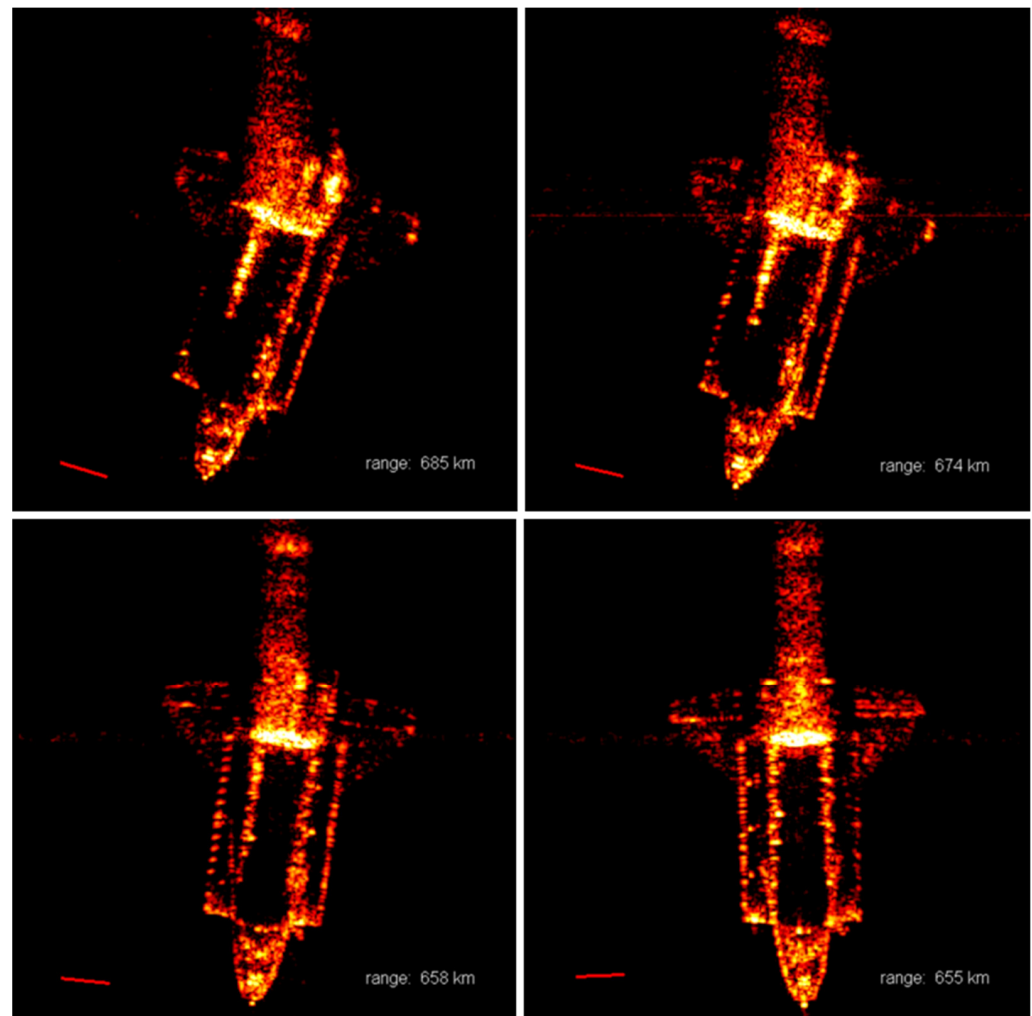


Figure 12. Wideband radar images of the USA Space Shuttle obtained by the TIRA (images courtesy of Fraunhofer FHR, Wachtberg, Germany).

There were many technological advancements enabling the development of HUSIR. A primary one was that of gyrotron amplifiers developed [59] by CPI. These gyrotrons employ superconducting magnets to generate an intense magnetic field in an oversized cylindrical interaction circuit, thus avoiding the electron beam clearance issues with the RF interaction region when attempting to extend coupled-cavity TWT designs to the W band. The W-band transmitter required a low-loss waveguide approximately 100 m long to convey RF power to the feed because the LRIR X-band transmitter and receiver fully occupied the RF box, which is located at the Cassegrain feed of the antenna. This was provided by corrugated over-moded waveguides [60] fabricated by General Atomics (GA), San Diego, CA USA. The power handling of this waveguide is also sufficient to handle the RF power upgrades described later without arcing. While microwave power tube transmitters have historically employed many other tubes in their high-voltage electronics (electron beam-switching tubes, thyatron crowbar triggers and regulator tubes), HUSIR provided a forum for the deployment of all-solid-state high-voltage power supplies and

modulators [61] by Diversified Technologies (DTI), Bedford, MA USA, for the gyrotron final power amplifier, and this arrangement has worked flawlessly for the past decade. The HUSIR receiver required development of cryogenically cooled low-noise amplifiers (LNAs), and these were provided [62] by the NASA Jet Propulsion Laboratory (JPL), Pasadena, CA USA. The ability of Lincoln Laboratory to partner with these industry and government colleagues was critical to the success of HUSIR and remains so as plans for further upgrades in capability move forward.

All this technological progress would have been hamstrung without a more capable antenna. The original Haystack antenna was a remarkable achievement for its time, and the RMS surface error (defined as half-path-length error) had been reduced from 0.64 mm RMS at the time of construction [52] to 0.21 mm RMS via a deformable subreflector [38]. This surface error was highly susceptible to deformation from the challenging thermal environment in the radome [63] and gravitational deformations, which are more severe in satellite tracking (due to the range of elevation involved) than celestial observations. A new antenna was required.

The new antenna, pictured in Figure 13, re-used the existing pedestal and hydrostatic azimuth bearing of the 1964 Haystack antenna, as well as the Y-shaped structure supporting the elevation bearings. The structural engineering was performed [64] by Simpson, Gumpertz and Heger (SGH), Waltham, MA USA. The deformations were quantified [65] to permit planning for necessary rigging and measurement campaigns upon construction. All antenna structures from the elevation bearings upward, including the 37 m diameter reflector, were replaced, along with drives and controls [66]. The engineering effort involved [52] was extraordinary. The space frame of the radome was retained, and the skin was replaced [67] to optimize transmission in the W band.

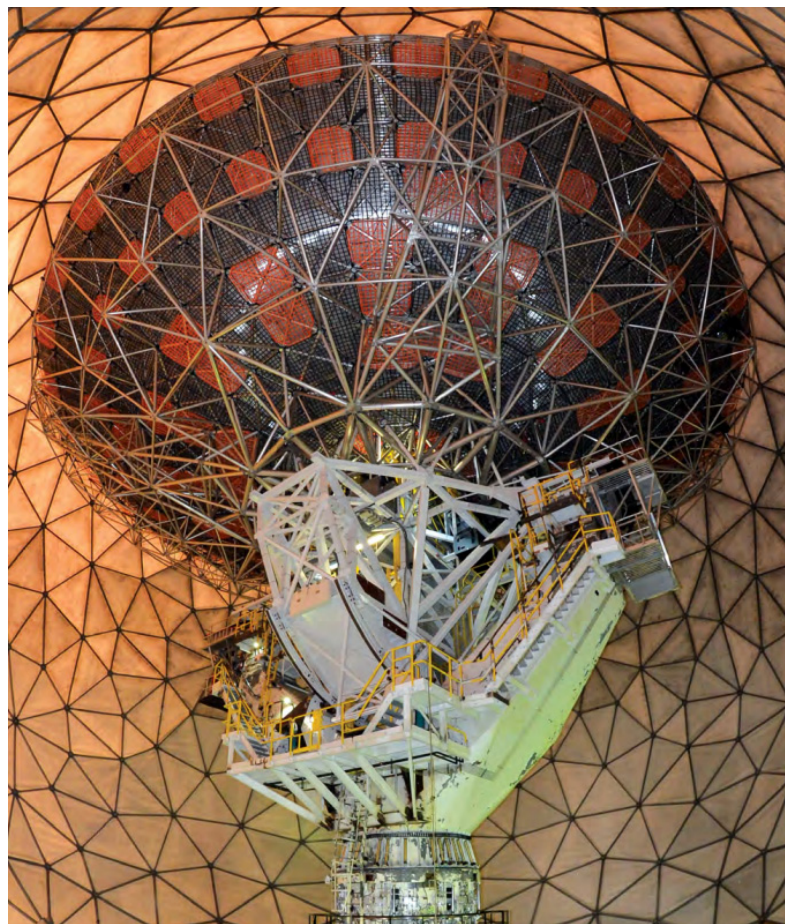


Figure 13. Cont.

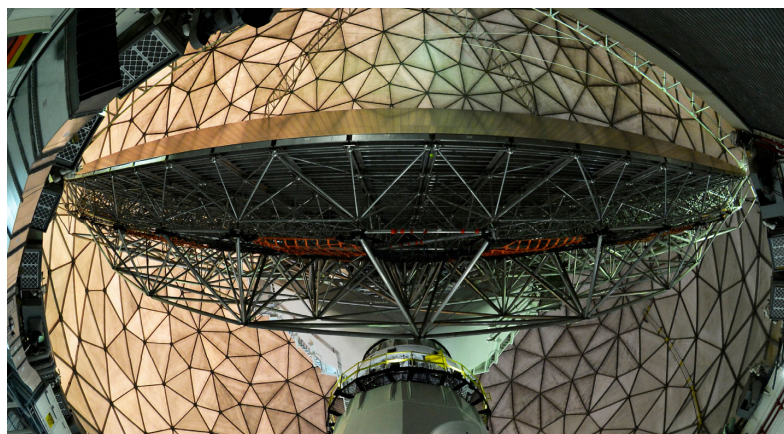


Figure 13. The Haystack Ultra-Wideband Satellite Imaging Radar (HUSIR) antenna. The backstructure and drives are seen at the top, while at the bottom, a “fisheye” lens photo provides a view of the reflector surface.

The demonstrated performance of the new antenna showed that the RMS surface error, after optimization [53], was 0.07 mm. Calibration procedures on Earth-orbiting satellites, with the repositioning of the subreflector, demonstrate radar sensitivity consistent with an antenna gain of 89 dB [52], the highest for a radar antenna in the world.

3. Upgrades in Progress and Future Plans

A brief summary of key parameters of the radars discussed in this paper is shown in Table 1. The radars described in this overview are often leveraged or used as technology testbeds in addition to their primary operational role. As is evident from the progress in capability over the past six decades, these radars are constantly evolving and being improved upon in modest and major ways. Some ongoing and upcoming efforts are summarized here.

Table 1. A summary of the parameters of the radars described here, in order of frequency.

Radar *	Construction	RF Parameters	Observation Parameters
MHR	25.6 m dia. antenna aperture 12-horn monopulse feed 42.6°N, 71.4°W	1.3 GHz center freq. 20 MHz bandwidth 3.0 MW peak power 300 kW average power *	50 dB reference SNR ** Deep space capable
Cobra Gemini-S	4.5 m dia. antenna aperture Compatible with radome Transportable	S band 300 MHz bandwidth 50 kW avg. power	0.8 m range accuracy
ALCOR	12.2 m dia. antenna aperture 4-horn monopulse feed 20.7 m dia. radome 9.4°N, 167.5°E	5.67 GHz center freq. 512 MHz bandwidth 3 MW peak power 6.0 kW average power	0.4 m range accuracy 100 urad angle accuracy 50 cm image resolution 23 dB reference SNR **
Cobra Gemini-X	4.5 m dia. antenna aperture Compatible with radome Transportable	X band 1 GHz bandwidth 35 kW avg. power	0.25 m range accuracy
LRIR/HUSIR-X	36.6 m dia. antenna aperture 4-horn monopulse feed 45.7 m dia. radome 42.6°N, 71.4°W	10.0 GHz center freq. 1 GHz bandwidth 400 kW peak power 120 kW average power	25 cm image resolution 53 dB reference SNR ** Deep space capable

Table 1. Cont.

Radar *	Construction	RF Parameters	Observation Parameters
HAX	12.2 m dia. antenna aperture 4 horn monopulse feed 20.7 m dia. radome 42.6°N, 71.4°W	16.7 GHz center freq. 2 GHz bandwidth 40 kW peak power	12 cm image resolution 36 dB reference SNR **
MMW	13.7 m dia. antenna aperture 4 horn monopulse feed 20.7 m dia. radome 9.4°N, 167.5°E	35 GHz center freq. 4 GHz bandwidth 60 kW peak power	40 urad angle accuracy 6 cm image resolution 26 dB reference SNR **
HUSIR-W	36.6 m dia. antenna aperture 4-horn monopulse feed 45.7 m dia. radome 42.6°N, 71.4°W	96 GHz center freq. 8 GHz bandwidth 1 kW peak power 400 W average power (50 kW Ppk in future *)	3 cm image resolution 34 dB reference SNR ** (Deep space cap. in future *)

* Asterisks indicate upgrades initiated at MIT Lincoln Laboratory. ** This SNR applies to a 1 m² (0 dBsm) RCS target at 1000 km range and can be scaled accordingly.

A recent upgrade at the Millstone Hill Radar [68] has constructed a completely new transmitter for the radar. Figures 14 and 15 show the new facility housing this transmitter, and one (of two) CPI VKL-7796 klystron and RF hardware. Two independent transmitters provide “hot spare” redundancy for improved sensor availability. A coolant plant providing 1.5 MW of heat-sinking capacity was included in the new facility.



Figure 14. The MHR antenna with the facility housing the new transmitter in the foreground.

High-voltage power and pulse modulation are provided by 92 series-connected solid-state rectifier and switch modules built by Ampegon Power Electronics AG, Baden, Switzerland. This architecture provides fault tolerance via bypass of any failed module and precise regulation of the pulse voltage. Fault currents in the event of an arc in the klystron are limited to less than 300 A to protect the transistors in the modules. This also limits the energy deposited in the klystron to a safe value.

The VKL-7796 doubles the average power of the previous klystron used at Millstone and provides increased RF bandwidth. It also provides commonality with other L-band radar transmitters to simplify procurement of klystron amplifiers.

In 2020, Lincoln Laboratory tasked CPI to develop a higher-power gyrotron [69] to serve as a final power amplifier for a 50 kW peak-power HUSIR W-band upgrade to extend the radar capability to geosynchronous range (40,000 km). This effort [70] also involves the redesign of the HUSIR W-band feed [71] to handle the increased power. Additionally, greater drive power from advanced solid-state amplifiers is needed [72] for the gyrotron to achieve its designed output.



Figure 15. The interior of the new transmitter facility with one of two klystrons (left) and its output waveguide and isolator (right). Coolant water is provided from the mezzanine level above.

The redesigned HUSIR feed, pictured in Figure 16, is being tested with the existing X-band feed. The integration of the X-band front end and W-band feed on the removable box allows planned maintenance to be conducted on the ground level with X-band radiation off a “splash plate” reflector oriented to send the radiation skyward during testing prior to re-insertion in the antenna. The ability to radiate in the W band simultaneously on the ground will be implemented in the near future upon addition of an RF switch and corrugated waveguide run to the test dock.

Development of the 50 kW GyroTWT at CPI is progressing, and the initial prototype unit is being tested as pictured in Figure 17. Early results obtained with W-band oscillators to drive the GyroTWT are in line with the predicted performance. More comprehensive testing with the tube operated in saturation at high-pulse duty has motivated the development of high-power solid-state amplifiers with sufficient gain to take the milliwatt power output of the HUSIR waveform generation hardware to 50 W or more, which is enough to saturate the GyroTWT across its full band. At the same time, these solid-state devices have to be protected from the possibility of RF burnout from an unintended oscillation of the tube. An interim drive capability has been brought to CPI in the form of a 20 W peak-power module fabricated by Raytheon Technologies using wideband MMIC devices developed [72] for HUSIR. These are combined in a “puck” architecture demonstrated by

Raytheon [73] over a narrower band. Isolation is provided by operating two HXI circulators developed for the HUSIR band in parallel to share the ~ 7 W average power. Raytheon has further combined eight such pucks [74] for what will ultimately be a 100 W HUSIR driver, providing sufficient power to saturate the tube through the 4 dB loss of the WARLOC duplexer which has been repurposed as an isolator.

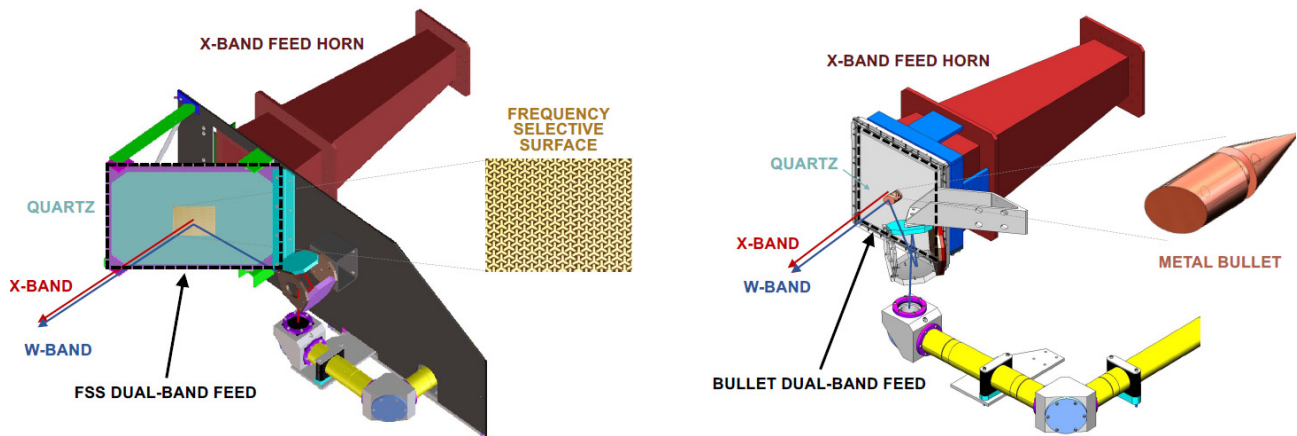


Figure 16. The HUSIR feed (left) and the new design for increased power (right).

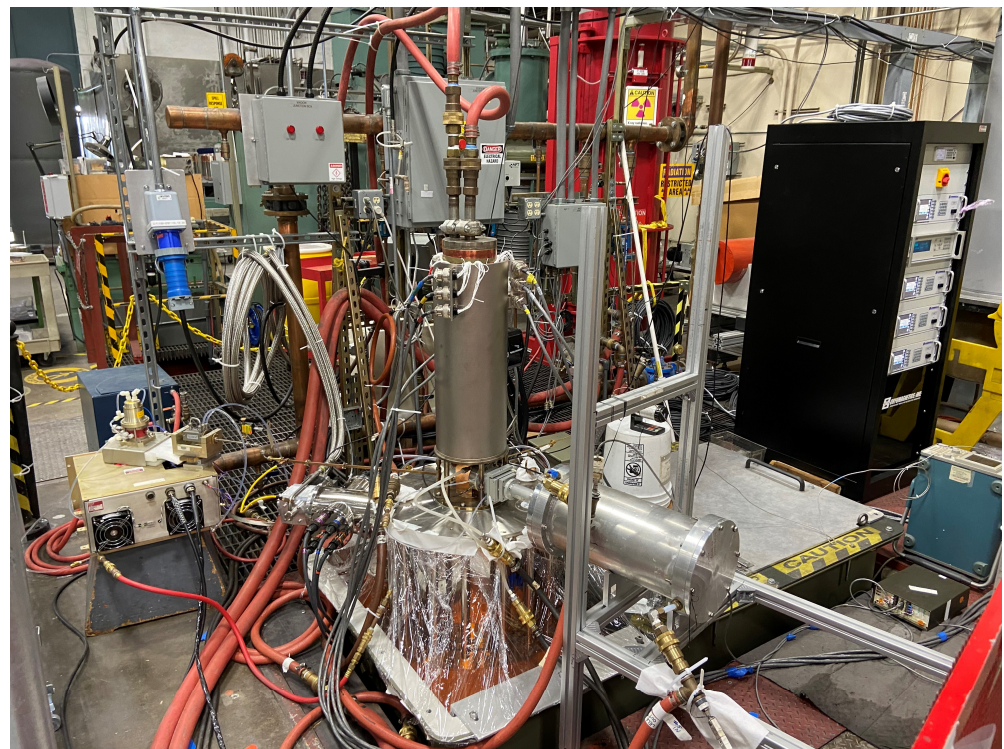


Figure 17. The 50 kW peak-power HUSIR gyroTWT mounted in a test stand at CPI.

Development of improved receiver protection technology is also underway at the Laboratory. The doubling of the average power of the Millstone transmitter motivated a new design for the reflective ionized-gas switch used in that radar as a duplexer. On transmit, a waveguide quadrature hybrid delivers high-power RF to two identical gas-filled sections of waveguide which are ionized by the transmit pulse and reflect the power onward to the antenna. On receive, the switches are no longer ionized, and RF passes through to the receiver.

A different scheme is used at HUSIR, where a wire grid polarizer is used to separate the transmit and receive paths, and this is followed by a three-stage latching circulator, il-

illustrated in Figure 18. The HUSIR receiver is cooled to 20 K, and this profoundly affects the design and testing of the latching circulators. These junction circulators employ a Y-shaped ferrite which is extremely small and difficult to fabricate and impedance-match. Improvements to the design, which will tolerate the 50-fold increase in HUSIR transmit power, are ongoing. Alternate methods such as high-speed switches are also being considered.



Figure 18. The cryogenic latching-circulator receiver protector for HUSIR (**left**) and its mounting in the 20 K dewar (**right**). The picture on the (**right**) shows mounting provisions for W-band receiver hardware, which is not installed in this picture.

Consideration is being given to further expanding the bandwidth of the MMW radar using frequency-multiplexing techniques developed at the Laboratory for other programs. Analyses and spectrum management considerations are in progress.

4. Discussion

The high-power radars that MIT Lincoln Laboratory has constructed and upgraded over nearly 70 years represent a significant national asset for the United States. Maintaining a commitment to continually improving their performance ensures that the observations they make will be supported in the long term, while new concepts provide a means of inserting advanced technology into this portfolio of sensors.

Figure 19, adapted from [36,51], illustrates the progress made in leveraging increased operating frequency and bandwidth to obtain progressively higher image resolution. As small payloads proliferate in space, and the debris population continues to grow, the need for long-range and wideband imaging sensors is becoming operationally critical for the US Space Force.

Figure 20 illustrates the challenge of keeping tabs on resident space objects as their population (including debris generated from collisions in orbit, unintentional and deliberate) continues to escalate dramatically, as seen in Figure 21. Over 12,000 spacecraft have been placed in orbit since 1957, of which more than 8000 remain. In 2014, NASA estimated the overall debris population to be over 500,000 (for sizes > 1 cm). In mid-2022, NASA also estimated [75] that there were over 25,000 objects on-orbit that are 10 cm or larger. In a 2020 report, the European Space Agency (ESA) estimated the 1 cm to 10 cm sized debris population at 100,000 and the 1 mm to 1 cm sized debris population at 130 million! Wideband radar sensors for space object imaging are complementary to optical sensors: at low Earth orbits, synoptic radar sensors (i.e., the US Space Force “Space Fence”) detect and track, while optical sensors can provide images. At long ranges, the roles are reversed, and optical sensors such as the Space Surveillance Telescope [76] provide synoptic data, while the range independence of radar image resolution (provided that a sufficient SNR exists to track the target) permits detailed target characterization in addition to target trajectory.

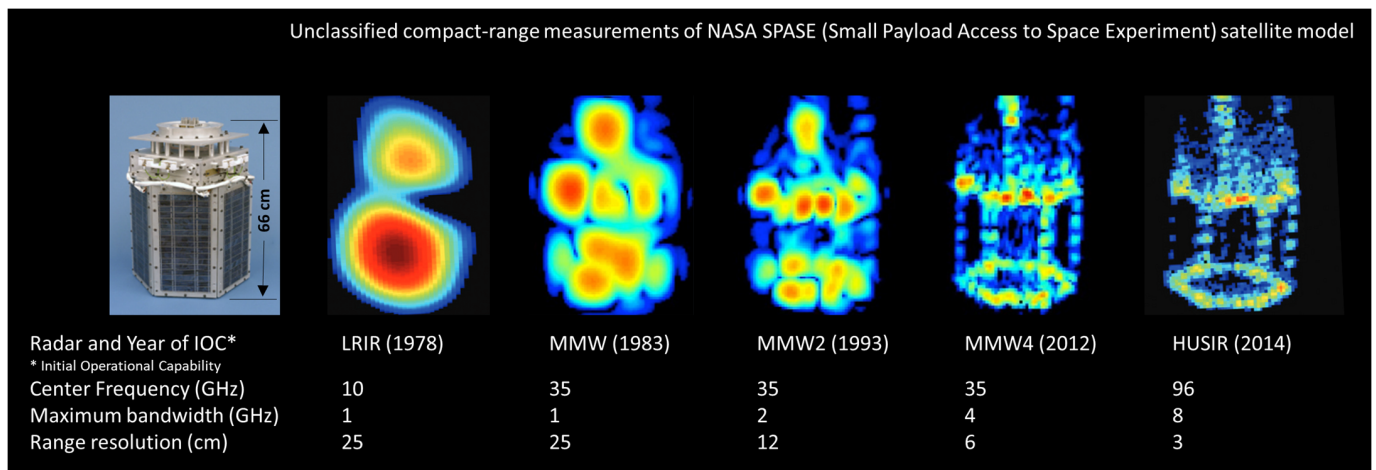


Figure 19. The progressive improvement in image resolution obtained at Lincoln Laboratory. Although ALCOR could image large objects, as seen in Figure 6, it is omitted from this chart, which focuses on the more recent need to image small orbiting payloads. Improved image resolution is achieved via increased radar waveform bandwidth, achieved both through increased center frequency with constant fractional bandwidth (e.g., HUSIR) and increased fractional bandwidth (e.g., MMW).

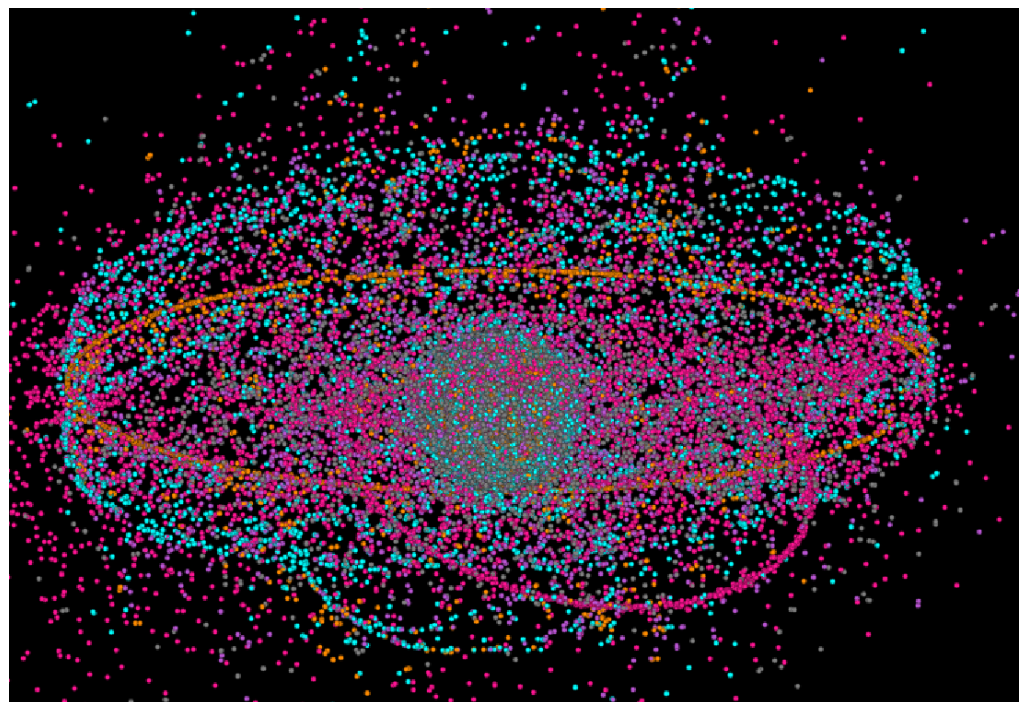


Figure 20. An illustration of the spatial distribution of man-made resident space objects about Earth (courtesy of AstriaGraph, University of Texas at Austin). Active satellites are color-coded in orange (the geostationary belt is clearly visible as an ellipse), inactive satellites in light blue, rocket bodies in violet and uncategorized objects in pink.

While this review has focused on activities at MIT Lincoln Laboratory, the broader radar community is actively meeting challenging mission scenarios in space. The need to improve space domain awareness, with emphasis on the geostationary orbit, motivated the Deep Space Advanced Radar Capability (DARC) technology demonstration [77] at Johns Hopkins Applied Physics Laboratory. This paves the way for an operational capability covering the entire geostationary belt jointly announced by the United States, Australia and the United Kingdom [78]. With NASA's commitment to return to the Moon, work has been undertaken [79] to use the NASA Deep Space Network radars to extend radar capability to

the cislunar region. These radars are also being exploited [80] for the characterization of asteroids. Lincoln Laboratory is also actively working in these areas, and the developments recounted here will continue to be extended to surmount the challenges of radar data collection for progressively smaller objects at ranges exceeding 40,000 km.

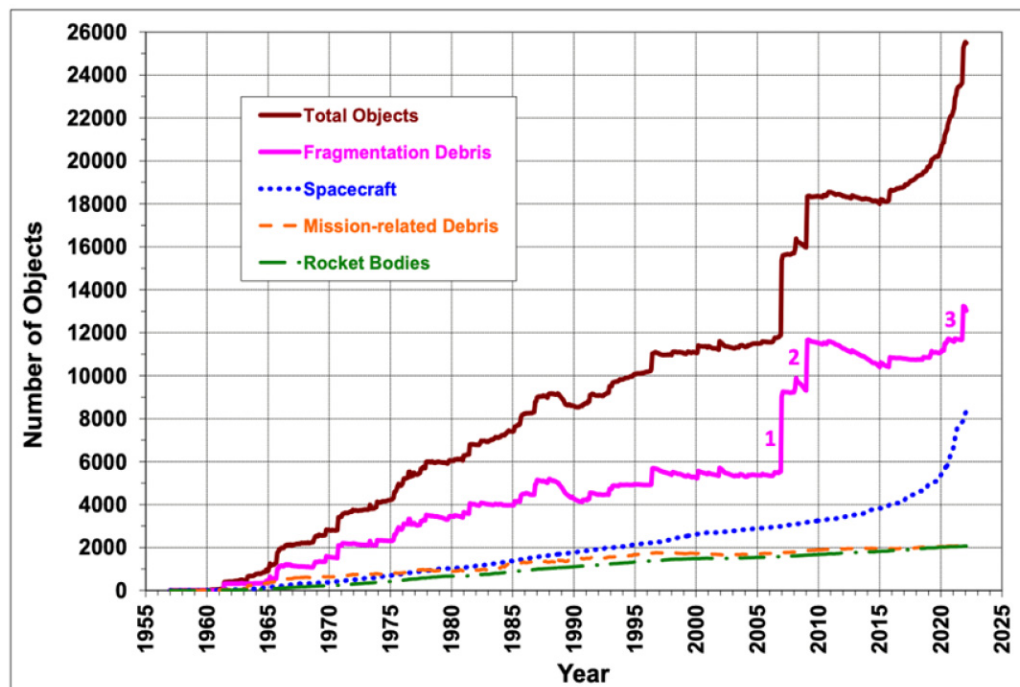


Figure 21. Reproduced from [75], the population of man-made resident space objects as a function of time. The numbered annotations show significant fragmentation events due to collisions in space, these being the 2007 Chinese anti-satellite (ASAT) test (1), the 2009 collision of Cosmos 2251 and Iridium 33 (2) and the 2013 Russian ASAT test (3).

Author Contributions: Resources and data curation, M.M., M.A. and J.S.; writing—original draft preparation, M.M., M.A. and J.S.; writing—review and editing, M.M. All authors have read and agreed to the published version of the manuscript.

Funding: This material is based on work supported by the Department of the Air Force under Air Force Contract No. FA8702-15-D-0001. Any opinions, findings, conclusions or recommendations expressed in this material are those of the author(s) and do not necessarily reflect the views of the Department of the Air Force. © 2024 Massachusetts Institute of Technology. Delivered to the US Government with Unlimited Rights, as defined in DFARS Part 252.227-7013 or 7014 (February 2014). Notwithstanding any copyright notice, US Government rights in this work are defined by DFARS 252.227-7013 or DFARS 252.227-7014 as detailed above. Use of this work other than as specifically authorized by the US Government may violate any copyrights that exist in this work. DISTRIBUTION STATEMENT A. Approved for public release. Distribution is unlimited.

Acknowledgments: In summarizing the breadth of work conducted at MIT Lincoln Laboratory over more than half a century, it is impossible to adequately acknowledge those who achieved these milestones. We have tried to capture as many contributors as possible, but much of the work is not in the open literature. In addition to the more than 80 Lincoln Laboratory authors cited here, we acknowledge the essential contributions of Gary Ahlgren, Gerry Banner, Bob Bergemann, Tom Clark, John Harris, V. Alexander Nedzel, Kurt Schwan, Paul Sebring, Grant Stokes, Henry Thomas and Lee Upton, as well as the financial support of the Defense Advanced Research Projects Agency, and the United States Army, Air Force and Space Force.

Conflicts of Interest: The authors declare no conflicts of interest.

References

1. Massachusetts Institute of Technology. *Radiation Laboratory Series (28 Volumes)*; Ridenour, L., Collins, G., Eds.; McGraw-Hill: New York, NY, USA, 2020; pp. 1948–1951. Available online: <https://archive.org/details/mit-rad-lab-series-version-2> (accessed on 9 March 2024).
2. *Technology in Support of National Security*; Grometstein, A. (Ed.) MIT Lincoln Laboratory: Lexington, MA, USA, 2011. Available online: https://www.ll.mit.edu/sites/default/files/other/doc/2018-04/MIT_Lincoln_Laboratory_history_book.pdf (accessed on 9 March 2024).
3. Ricardi, L.; Niro, L. Design of a 12-horn monopulse feed. In Proceedings of the 1958 IRE International Convention Record, New York, NY, USA, 21–25 March 1966; pp. 49–56. [CrossRef]
4. Millstone Hill Incoherent Scatter Radar. Available online: <https://www.haystack.mit.edu/about/haystack-telescopes-and-facilities/millstone-hill-incoherent-scatter-radar/> (accessed on 9 March 2024).
5. Evans, J. Theory and practice of ionosphere study by Thomson scatter radar. *Proc. IEEE* **1969**, *57*, 496–530. [CrossRef]
6. Pensa, A. Historical Perspective. In *Perspectives in Space Surveillance*; Sridharan, R., Pensa, A., Eds.; MIT Press: Cambridge, MA, USA, 2017; pp. 1–13.
7. Sridharan, R.; Kupiec, I. Technology Development for Space Surveillance with Narrow-beam Radars. In *Perspectives in Space Surveillance*; Sridharan, R., Pensa, A., Eds.; MIT Press: Cambridge, MA, USA, 2017; pp. 15–73.
8. Welch, S.; Hogan, G.; Morrison, R.; Bassa, C.; Pisano, T. Long baseline radar bistatic measurements of geostationary satellites. In Proceedings of the 2022 19th European Radar Conference (EuRAD), Milan, Italy, 28–30 September 2022; pp. 17–20. [CrossRef]
9. Ruze, J. Antenna tolerance theory—a review. *Proc. IEEE* **1965**, *54*, 633–640. [CrossRef]
10. Weiss, H. The Millstone and Haystack radars. *IEEE Trans. Aerosp. Elect. Syst.* **2001**, *37*, 365–379. [CrossRef]
11. Whitney, A.; Lonsdale, C.; Fish, V. Insights into the Universe: Astronomy with Haystack’s radio telescope. *Linc. Lab. J.* **2014**, *21*, 8–27. Available online: https://archive.ll.mit.edu/publications/journal/pdf/vol21_no1/21_1_2_Whitney.pdf (accessed on 9 March 2024).
12. Shapiro, I.; Pettengill, G.; Ash, M.; Stone, M.; Smith, W.; Ingalls, R.; Brockelman, R. Fourth test of General Relativity: Preliminary results. *Phys. Rev. Lett.* **1968**, *20*, 1265–1269. [CrossRef]
13. Delaney, W.; Ward, W. Radar development at Lincoln Laboratory: An overview of the first fifty years. *Linc. Lab. J.* **2000**, *12*, 147–166. Available online: https://archive.ll.mit.edu/publications/journal/pdf/vol12_no2/12_2radardevelopment.pdf (accessed on 9 March 2024).
14. Roth, K.; Austin, M.; Frediani DKnittel, G.; Mrstik, A. The Kiernan re-entry measurements system at Kwajalein Atoll. *Linc. Lab. J.* **1989**, *2*, 247–276. Available online: https://archive.ll.mit.edu/publications/journal/pdf/vol02_no2/2.2.7.kiernanreentry.pdf (accessed on 9 March 2024).
15. Avent, R.; Shelton, J.; Brown, P. The ALCOR C-band imaging radar. *IEEE Antennas Prop. Mag.* **1996**, *38*, 16–27. [CrossRef]
16. Skolnik, M. (Ed.) *Introduction to Radar Systems*, 2nd ed.; McGraw-Hill: New York, NY, USA, 1980.
17. Axelbank, M.; Camp, W.; Lynn, V.; Margolin, J. ALCOR: A high-sensitivity radar with one-half meter range resolution. In Proceedings of the 1971 IEEE International Convention Digest, New York, NY, USA, 22–25 March 1971; pp. 112–113.
18. Purdy, R.; Blankenship, P.; Muehe, C.; Rader, C.; Stern, E.; Williamson, R. Radar signal processing. *Linc. Lab. J.* **2000**, *12*, 297–320. Available online: https://archive.ll.mit.edu/publications/journal/pdf/vol12_no2/12_2radarsignalprocessing.pdf (accessed on 9 March 2024).
19. Camp, W.; Mayhan, J.; O’Donnell, R. Wideband Radar for Ballistic Missile Defense and Range-Doppler Imaging of Satellites. *Linc. Lab. J.* **2000**, *12*, 267–280. Available online: https://archive.ll.mit.edu/publications/journal/pdf/vol12_no2/12_2widebandradar.pdf (accessed on 9 March 2024).
20. Solodyna, C. Overview of Wideband Imaging Radar Technology. In *Perspectives in Space Surveillance*; Sridharan, R., Pensa, A., Eds.; MIT Press: Cambridge, MA, USA, 2017; pp. 75–117.
21. Brown, W.; Pensa, A. History of Haystack. *Linc. Lab. J.* **2014**, *21*, 4–7. Available online: https://archive.ll.mit.edu/publications/journal/pdf/vol21_no1/21_1_1_Brown.pdf (accessed on 9 March 2024).
22. James, B.; Zitelli, L. A 100 kW peak 50 kW average coupled cavity TWT with 10% bandwidth centered at 10 GHz. In Proceedings of the IEEE Electron Devices Meeting, Washington, DC, USA, 1–2 December 1975; p. 133. [CrossRef]
23. Goudey, K.; Sciambi, A. High power X-band monopulse tracking feed for the Lincoln Laboratory Long Range Imaging Radar. *IEEE Trans. Microw. Theory Tech.* **1978**, *26*, 326–332. [CrossRef]
24. Goldie, H. A 2-kilowatt average power X-band receiver protector. *IEEE Trans. Electron. Dev.* **1977**, *24*, 53–55. [CrossRef]
25. Bromaghim, D.; Perry, J. A wideband FM linear ramp generator for the Long-Range Imaging Radar. *IEEE Trans. Microw. Theory Tech.* **1978**, *26*, 322–325. [CrossRef]
26. Sangiolo, T.; Spence, L. PACS: A processing and control system for the Haystack Long-range Imaging Radar. In Proceedings of the 1990 IEEE International Conference on Radar, Arlington, VA, USA, 7–10 May 1990; pp. 480–485. [CrossRef]
27. Abouzahra, M.; Avent, R. The 100-kW millimeter wave radar at the Kwajalein Atoll. *IEEE Antennas Prop. Mag.* **1994**, *36*, 7–19. [CrossRef]
28. Ingwersen, P.; Lemnios, W. Radars for ballistic missile defense research. *Linc. Lab. J.* **2000**, *12*, 245–266. Available online: https://archive.ll.mit.edu/publications/journal/pdf/vol12_no2/12_2ballisticmissiledefense.pdf (accessed on 9 March 2024).

29. Hall, T.; Duff, G.; Maciel, L. The space mission at Kwajalein. *Linc. Lab. J.* **2012**, *19*, 48–63. Available online: https://archive.ll.mit.edu/publications/journal/pdf/vol19_no2/19_2_3_Hall.pdf (accessed on 9 March 2024).
30. Fitzgerald, W. A 35 GHz beam waveguide system for the Millimeter Wave Radar. *Linc. Lab. J.* **1992**, *5*, 245–272. Available online: https://archive.ll.mit.edu/publications/journal/pdf/vol05_no2/5.2.4.35ghzwaveguide.pdf (accessed on 9 March 2024).
31. Dionne, G. Laboratory-scale mirrors for submillimeter wavelengths. *Int. J. Infrared Millim. Waves* **1982**, *3*, 417–423. [CrossRef]
32. Goldsmith, P. *Quasioptical Systems*; IEEE Press: New York, NY, USA, 1998.
33. Dionne, G.; Weiss, A.; Allen, G. Non-reciprocal magneto-optics for millimeter waves. *IEEE Trans. Magn.* **1988**, *24*, 2817–2819. [CrossRef]
34. McHarg, J.; Abouzahra, M.; Lucey, R. 95-GHz Millimeter-wave Radar. In *Millimeter and Submillimeter Waves Appl. III, Proceedings of the 1996 SPIE International Symposium on Optical Science, Engineering and Instrumentation, Denver, CO, USA, 5–9 August 1996*; SPIE: Denver, CO, USA, 1996; Volume 2842, pp. 494–500. [CrossRef]
35. Linde, G.; Ngo, M.; Danly, B.; Cheung, W.; Gregers-Hansen, V. WARLOC: A high-power coherent 94 GHz radar. *IEEE Trans. Aerosp. Elect. Sys.* **2008**, *44*, 1102–1117. [CrossRef]
36. Stambaugh, J.; Lee, R.; Cantrell, W. The 4 GHz bandwidth Millimeter Wave Radar. *Linc. Lab. J.* **2012**, *19*, 64–76. Available online: https://archive.ll.mit.edu/publications/journal/pdf/vol19_no2/19_2_4_Stambaugh.pdf (accessed on 9 March 2024).
37. Jones, G.; Abouzahra, M. Major improvements at the KREMS Millimeter Wave Radar. In *Proceedings of the 1992 Space Surveillance Workshop, Lexington, MA, USA, 7–9 April 1992*; pp. 239–244.
38. Ingalls, R.; Antebi, J.; Ball, J.; Barvainis, R.; Cannon, J.; Carter, J.; Charpentier, P.; Corey, B.; Crowley, J.; Dudevoir, K.; et al. Upgrading the Haystack radio telescope for operation at 115 GHz. *Proc. IEEE* **1994**, *82*, 742–755. [CrossRef]
39. Stansbery, E.; Settecerri, T. A Comparison of Haystack and HAX measurements of the orbital debris environment. In *Proceedings of the Second European Conference on Space Debris, Organised by ESA, Darmstadt, Germany, 17–19 March 1997*; ESOC: Darmstadt, Germany, 1997. ESA-SP 393. p. 59.
40. Robinson, P.; North, W. Compact floating-deck modulator for the HAX transmitter. In *Proceedings of the Twentieth Conference Record on Power Modulator Symposium, Myrtle Beach, SC, USA, 23–25 June 1992*; pp. 41–44. [CrossRef]
41. James, B. Re-Entrant Double-Staggered Ladder Circuit. U.S. Patent 4866343A, 12 September 1989.
42. Corbett, E.; Rossini, P.; Gallon, D.; Hotz, A. Pointing and tracking servo for the Haystack Auxiliary antenna (HAX). In *Proceedings of the First IEEE Conference on Control Applications, Dayton, OH, USA, 13–16 September 1992*; Volume 2, pp. 1134–1139. [CrossRef]
43. Available online: <https://orbitaldebris.jsc.nasa.gov/measurements/radar.html> (accessed on 9 March 2024).
44. Ruiz, G.; Patzelt, T.; Leuschake, L.; Loffeld, O. Autonomous tracking of space objects with the FGAN tracking and imaging radar. In *Proceedings of the Informatik 2006—Informatik für Menschen, Band 1, Bonn: Gesellschaft für Informatik e.V., Dresden, Germany, 2–6 October 2006*; pp. 349–353. Available online: <https://dl.gi.de/handle/20.500.12116/23700> (accessed on 9 March 2024).
45. Karamanavis, V.; Dirks, H.; Fuhrmann, L.; Schlichthaber, F.; Egli, N.; Patzelt, T.; Klare, J. Characterization of deorbiting satellites and space debris with radar. *Adv. Sp. Res.* **2023**, *72*, 3269–3281. [CrossRef]
46. Mayhan, J.; O'Donnell, W.; Willner, D. The Cobra Gemini radar. In *Proceedings of the 1996 IEEE National Radar Conference, Ann Arbor, MI, USA, 13–16 May 1996*; pp. 380–385. [CrossRef]
47. Rejto, S. Radar open systems architecture and applications. In *Proceedings of the IEEE 2000 International Radar Conference, Alexandria, VA, USA, 12 May 2000*; pp. 654–659. [CrossRef]
48. Nelson, J. Radar open system architecture provides net centricity. *IEEE Aerosp. Elect. Syst. Mag.* **2010**, *25*, 17–20. [CrossRef]
49. MIT Lincoln Laboratory. 2012 Annual Report, Page 17. Available online: https://archive.ll.mit.edu/publications/Annual_Report_2012.pdf (accessed on 9 March 2024).
50. Missile Defense Agency. Flight Test Infrastructure Data Sheet, SS Pacific Tracker, 16-MDA-8889, Attachment 5. 14 October 2016. Available online: <https://govtribe.com/file/government-file/mda17dtrfi01-attachment-5-xtr-1-tts-2-fact-sheet-dot-pdf> (accessed on 9 March 2024).
51. Czerwinski, M.; Usoff, J. Development of the Haystack Ultrawideband Satellite Imaging Radar. *Linc. Lab. J.* **2014**, *21*, 28–44. Available online: https://archive.ll.mit.edu/publications/journal/pdf/vol21_no1/21_1_3_Czerwinski.pdf (accessed on 9 March 2024).
52. Waggener, N. Construction of the HUSIR antenna. *Linc. Lab. J.* **2014**, *21*, 45–82. Available online: https://archive.ll.mit.edu/publications/journal/pdf/vol21_no1/21_1_5_Waggener.pdf (accessed on 9 March 2024).
53. Usoff, J.; Clarke, M.; Liu, C.; Silver, M. Optimizing the HUSIR antenna surface. *Linc. Lab. J.* **2014**, *21*, 83–105. Available online: https://archive.ll.mit.edu/publications/journal/pdf/vol21_no1/21_1_6_Usoff.pdf (accessed on 9 March 2024).
54. MacDonald, M.; Anderson, J.; Lee, R.; Gordon, D.; McGrew, G. The HUSIR W-band transmitter. *Linc. Lab. J.* **2014**, *21*, 106–114. Available online: https://archive.ll.mit.edu/publications/journal/pdf/vol21_no1/21_1_4_MacDonald.pdf (accessed on 9 March 2024).
55. Eshbaugh, J.; Morrison, R.; Hoen, E.; Hiatt, T.; Benitz, G. HUSIR signal processing. *Linc. Lab. J.* **2014**, *21*, 115–133. Available online: https://archive.ll.mit.edu/publications/journal/pdf/vol21_no1/21_1_7_Eshbaugh.pdf (accessed on 9 March 2024).
56. Kauffman, J.; Rajagopalan, G.; Akiyama, K.; Fish, V.; Lonsdale, C.; Matthews, L.; Pillai, T. The Haystack telescope as an astronomical instrument. *Galaxies* **2023**, *11*, 9. [CrossRef]

57. Jacobs, J.; Kennedy, T. *Haystack Ultra-Wideband Satellite Imaging Radar Measurements of the Orbital Debris Environment: 2018*; NASA/TP-2020-5006606; National Aeronautics and Space Administration: Washington, DC, USA, 2018.
58. Rodenbeck, C.; Tierney, B.; Park, J.; Parent, M.; Depuma, C.; Bauder, C.; Pizzillo, T.; Jaffe, P.; Simakauskas, B.; Mayhan, T. Terrestrial microwave power beaming. *IEEE J. Microw.* **2021**, *2*, 28–43. [[CrossRef](#)]
59. Blank, M.; Borchard, P.; Cauffman, S.; Felch, K. Design and demonstration of W-band gyrotron amplifiers for radar applications. In Proceedings of the 2007 Joint 32nd International Conference on Infrared and Millimeter Waves, Cardiff, UK, 2–9 September 2007; pp. 358–361. [[CrossRef](#)]
60. Doane, J. Propagation and Mode Coupling in Corrugated and Smooth-wall Circular Waveguides, Ch. 5. In *Infrared and Millimeter Waves, Vol. 13, Millimeter Components and Techniques, Part IV*; Button, K., Ed.; Academic Press: Orlando, FL, USA, 1985.
61. Kempkes, M.; Hawkey, T.; Gaudreau, M.; Phillips, R. W-band transmitter upgrade for the Haystack Ultra-wideband Satellite Imaging Radar. In Proceedings of the 2006 IEEE International Vacuum Electronics Conference held Jointly with 2006 IEEE International Vacuum Electron Sources, Monterey, CA, USA, 25–27 April 2006; pp. 551–552. [[CrossRef](#)]
62. Maiwald, F.; Lin, R.; Dengler, R.; Smith, S.; Pearson, J.; Mehdi, I.; Gaier, T.; Crowley, J. High output power low noise amplifier chains at 100 GHz. In Proceedings of the 18th International Symposium on Space Terahertz Technology, Pasadena, CA, USA, 21–23 March 2007; pp. 131–134.
63. MacDonald, M. Measured thermal dynamics of the HUSIR antenna and Haystack Radome. *IEEE Trans. Antennas Prop.* **2013**, *61*, 2441–2448. [[CrossRef](#)]
64. Antebi, J.; Kan, F. Replacement of elevation structure to upgrade Haystack 37-m radio telescope. In Proceedings of the Astronomical Structures and Mechanisms Technology, Glasgow, UK, 21–22 June 2004; Volume 5495. [[CrossRef](#)]
65. Doyle, K.; Brenner, M.; Antebi, J.; Kan, F.; Valentine, D. RF-mechanical performance for the Haystack radio telescope. In Proceedings of the SPIE Optical Engineering + Applications, San Diego, CA, USA, 24 September 2011; Volume 8125. [[CrossRef](#)]
66. Eshbaugh, J.; Clarke, M.; Maglathlin, G. Haystack Antenna Control System Design Document. Project Report HUSIR-8, MIT Lincoln Laboratory, Defense Technical Information Center Report ESC-TR-2010-071. 7 December 2010. Available online: <https://apps.dtic.mil/sti/tr/pdf/ADA533478.pdf> (accessed on 9 March 2024).
67. MacDonald, M. An overview of radomes for large ground-based antennas. *IEEE Aerosp. Elect. Syst. Mag.* **2019**, *34*, 36–43. [[CrossRef](#)]
68. Beals, D.; Abouzahra, M.; Schoenfeld, M.; MacGibbon, P. Millstone Hill Radar L-band sensitivity upgrade. In Proceedings of the 2023 International Applied Computational Electromagnetics Society Symposium (ACES), Monterey/Seaside, CA, USA, 26–30 March 2023; pp. 1–2. [[CrossRef](#)]
69. Grimes, D.; MacDonald, M. Enabling deep space radar with EM simulation. In Proceedings of the 2023 International Applied Computational Electromagnetics Society Symposium (ACES), Monterey/Seaside CA, USA, 26–30 March 2023; pp. 1–2. [[CrossRef](#)]
70. Abouzahra, M.; MacDonald, M.; Lee, R.; Grimes, D.; Simakauskas, B.; Lopez, N.; Eckert, C.; Usoff, J. Upgrading the HUSIR radar for deep-space satellite imaging. In Proceedings of the 2022 IEEE/MTT-S International Microwave Symposium—IMS 2022, Denver, CO, USA, 19–24 June 2022; pp. 429–432. [[CrossRef](#)]
71. Lee, R.; Simakauskas, B.; Eckert, C.; Abouzahra, M. Development of the HUSIR dual-band feed. In Proceedings of the 2022 19th European Radar Conference (EuRAD), Milan, Italy, 28–30 September 2022; pp. 29–32. [[CrossRef](#)]
72. Lopez, N.; MacDonald, M.; Abouzahra, M. LSSC Solid-state high-power amplifiers. In Proceedings of the 2022 19th European Radar Conference (EuRAD), Milan, Italy, 28–30 September 2022; pp. 25–28. [[CrossRef](#)]
73. Soric, J.; Koliass, N.; Saunders, J.; Kotce, J.; Brown, A.; Rodenbeck, C.; Gyurcsik, R. A 100-Watt GaN SSPA. *IEEE Microw. Wirel. Comp. Lett.* **2022**, *32*, 712–715. [[CrossRef](#)]
74. Soric, J.; Koliass, N.; Saunders, J.; Kotce, J.; Gyurcsik, R.; Abouzahra, M.; MacDonald, M. A 92–100 GHz 100 W SSPA for the HUSIR Deep-Space Upgrade. In Proceedings of the 54th European Microwave Conference (EuMC), Paris, France, 22–27 September 2024. (In press).
75. Available online: <https://orbitaldebris.jsc.nasa.gov/quarterly-news/pdfs/odqnv26i1.pdf> (accessed on 9 March 2024).
76. Available online: <https://spacenews.com/space-surveillance-telescope-developed-by-the-u-s-begins-operations-in-australia/> (accessed on 9 March 2024).
77. Available online: <https://www.jhuapl.edu/work/projects/deep-space-advanced-radar-capability-darc-technology-demonstration> (accessed on 9 March 2024).
78. Available online: <https://www.spaceforce.mil/News/Article-Display/Article/3604036/> (accessed on 9 March 2024).
79. Lee, C.; Rodriguez-Alvarez, N.; Giorgini, J.D.; Jao, J.S.; Majid, W.; Naudet, C.J.; Oudrhiri, K.; Yang, Y.-M. Cis-lunar space debris radar capability and feasibility. In Proceedings of the 2023 IEEE Aerospace Conference, Big Sky, MT, USA, 4–11 March 2023. [[CrossRef](#)]
80. Available online: <http://echo.jpl.nasa.gov/> (accessed on 9 March 2024).

Disclaimer/Publisher’s Note: The statements, opinions and data contained in all publications are solely those of the individual author(s) and contributor(s) and not of MDPI and/or the editor(s). MDPI and/or the editor(s) disclaim responsibility for any injury to people or property resulting from any ideas, methods, instructions or products referred to in the content.